ISSN 0020-1685, Inorganic Materials, 2023, Vol. 59, No. 2, pp. 145–156. © Pleiades Publishing, Ltd., 2023.
ISSN 0020-1685, Inorganic Materials, 2023. © Pleiades Publishing, Ltd., 2023.
Russian Text © The Author(s), 2023, published in Neorganicheskie Materialy, 2023, Vol. 59, No. 2, pp. 150–161.

Synthesis of Titanium Oxide/Manganese Oxide Composites and Their Physicochemical and Photocatalytic Properties

M. L. Belikov[a], *, S. A. Safaryan[a], and P. A. Korneikova[a]

[a] *Tananaev Institute of Chemistry and Technology of Rare Elements and Minerals (separate subdivision), Kola Scientific Center (Federal Research Center), Russian Academy of Sciences, Apatity, Murmansk oblast, 184209 Russia*

**e-mail: masim-bek@mail.ru*

Received June 15, 2022; revised December 6, 2022; accepted December 8, 2022

Abstract—We have synthesized photocatalytically active manganese-modified titanium dioxide-based materials and studied key features of the formation of the synthesized materials and their physicochemical and photocatalytic properties. Modification of TiO_2 with manganese has been shown to ensure preparation of nanopowders (4.8–2550 nm) with a specific free surface area from 0.56 to 479 m^2/g. The synthesized powders have high photocatalytic activity (PCA) under illumination with visible light, which exceeds the PCA of unmodified TiO_2 of the same origin and that of Degussa P-25 commercially available titanium dioxide. An increased PCA level is offered by the manganese-modified materials containing both anatase and rutile, without separation of individual manganese phases.

Keywords: synthesis, titanium dioxide, manganese, photocatalytic activity, visible light

DOI: 10.1134/S0020168523020024

INTRODUCTION

Titanium dioxide as a photocatalytically active material attracted particular attention in the early 1970s after a report by Fujishima and Honda [1], who demonstrated the feasibility of photocatalytic water splitting in the presence of TiO_2. Having high photocatalytic activity (PCA), TiO_2 turned out to be highly effective in degrading many organic pollutants [2–5], including various microbiotas [6–8].

In addition to TiO_2, a variety of semiconductor materials are regarded and used as photocatalysts: ZnO, WO_3, Fe_2O_3, CdSe, $SrTiO_3$, SiC, CdS, GaP, GaAs, and others [9–21]. Nevertheless, among the many photocatalytic materials, only titanium dioxide combines a number of necessary properties: high PCA; physical, chemical, and biological stability; availability; and nontoxicity [2, 22].

Having many advantages, pure titanium dioxide exhibits photocatalytic activity only under ultraviolet irradiation, because it has a rather large band gap (E_g = 3.2 eV in anatase and 3.0 eV in rutile), which leads to an additional energy loss, since the fraction of UV light in the solar spectrum is just 3–7% [23–26]. This limits the utility of TiO_2 as a photocatalyst under illumination at wavelengths $\lambda > 400$ nm. The spectral range of titanium dioxide photosensitivity can be extended to longer wavelengths by adding various modifiers capable of reducing the E_g of TiO_2. For example, the E_g of manganese oxide is 1.25 eV, against 3.2 eV in titanium dioxide.

Composites based on polycrystalline Mn^{2+}-modified titanium dioxide are known to have increased PCA for aniline blue decomposition under UV irradiation [28]. Modification with Mn^{2+} ions was shown to promote the anatase-to-rutile transformation and shift the photoabsorption edge of TiO_2 to the visible spectral region. The presence of Mn^{2+} ions (0.06 at %) in TiO_2 caused an increase in its PCA, which was accounted for by a synergetic effect between anatase and rutile [29].

As shown by Brus et al. [30] and Ivanova and Harizanova [31], increasing the percentage of manganese oxide in titanium oxide (from 0 to 5 wt %) reduces its E_g, which should lead to a shift of its photosensitivity to longer wavelengths.

Modification of TiO_2 with tungsten was shown to raise its electrical conductivity by two orders of magnitude [32]. An increase in the electrical conductivity of an oxide material as a consequence of incorporation of a modifying additive can be interpreted as an indication of an increase in its PCA. In particular, an increase in the degree of TiO_2 modification with an aliovalent metal was shown to lead to an increase in the

electrical conductivity of the material [33], which correlates with PCA data.

As shown by Jin et al. [34], manganese modification of P-25 commercially available titanium dioxide (Degussa) leads to an increase in its PCA.

They believe that alkaline cohydrolysis of water-soluble titanium and manganese salts, a simple and effective method, can ensure preparation of photocatalysts in a wide range of manganese modifier contents (from 1 to 30 wt %).

The purpose of this work was to synthesize photocatalytically active materials based on Mn-modified titanium dioxide and to study their physicochemical and photocatalytic properties under illumination with visible light

EXPERIMENTAL

Photocatalytic materials were prepared through alkaline cohydrolysis of a titanium salt ($TiCl_4$ or $TiOSO_4 \cdot xH_2O$) and $MnCl_2$ in a NH_4OH solution (120 g/L) as described previously [35, 36]. During the hydrolysis process, the solution temperature did not exceed 40°C. All of the chemicals used were of reagent grade.

After settling of the resultant suspension, the precipitate was washed with a copious amount of distilled water. The variable process parameters were the degree of titanium dioxide modification with manganese (1–30 wt %) and the temperature at which the precipitates obtained were heat-treated in air for 1 h (80 to 800°C). The heating/cooling rate was 15°C/min, and the holding time at a given temperature was 60 min.

The synthesis products were characterized by low-temperature nitrogen adsorption BET measurements (FlowSorb II 2300 and TriStar 3020 V1.03), thermogravimetry (TG) in an argon atmosphere at a heating rate of 10°C/min in a Stepanov vessel with the use of a sheathed Pt/Pt–Rh thermocouple (Netzsch STA 409 PC/PG), chemical analysis, and X-ray diffraction (XRD) (DRON-2 diffractometer, CuK_α radiation).

PCA (E, %) was assessed photocolorimetrically with an SF-56 spectrophotometer from the degree of decoloration of aniline (C_0 = 100 mg/L), ferroin (C_0 = 100 mg/L), or methylene blue (MB) (C_0 = 50 mg/L) solutions under illumination with visible light. The illuminance, monitored with a TKA-PKM (06) combined device (luxmeter + UV radiometer) was 2300 lx. The effectiveness of dye decomposition as a measure of PCA (E, %) was evaluated using the relation

$$E = [(C_0 - C_f)/C_0] \times 100\%, \quad (1)$$

where C_0 (mg/L) is the initial dye concentration in solution and C_f (mg/L) is the final dye concentration in solution.

The reference materials used were TiO_2 of the same origin as the manganese-modified TiO_2 and commercially available Degussa TiO_2 (P-25, Degussa AG, Frankfort, Germany), which had been proposed previously as a reference standard [37]. The samples were identified by a code, for example, 800-Mn-5, which specified the heat-treatment temperature (800°C), the modifying metal (Mn), and its percentage in the material (5 wt %).

RESULTS AND DISCUSSION

Tables 1–4 and Figs. 1–7 summarize the present experimental data on the chemical and phase compositions (XRD), specific surface area (S, m^2/g), and average particle size (d, nm) of the synthesis products and the pore depth (h, nm) and diameter (D, nm) as functions of heat treatment conditions (t, °C) and Mn concentration (wt %) in the final product and also on the degree of PCA (E, %) for dye destruction under illumination with visible light.

Manganese chloride hydrolysis and the formation of a precipitate in aqueous ammonia, accompanied by the formation of a titanium hydroxide precipitate, is a

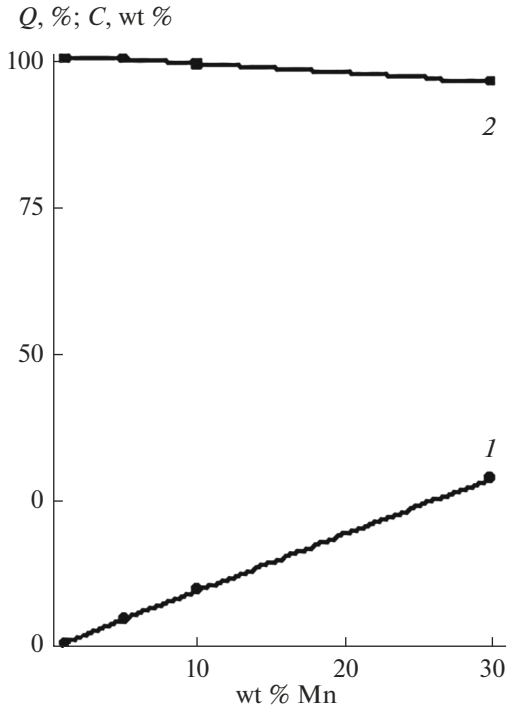

Fig. 1. Dependences of (*1*) the percentage of Mn (C) in the samples and (*2*) Mn extraction into the precipitate (Q) as a result of ammonia hydrolysis.

Table 1. Physicochemical properties of TiO_2 and Mn-modified samples

Sample	*t*, °C	Weight percent				XRD	*S*, m^2/g	*d*, nm
		TiO_2	Cl^-	NH_4^+	Mn^{3+}		BET	
80-TiO_2	80	79.8	1.06	2.84	0	am	270.0	8.54
300-TiO_2	300	–	–	–	–	am	258.8	8.9
400-TiO_2	400	98.5	0.06	0.42	0	am	155.4	9.90
500-TiO_2	500	–	–	–	–	a	52.4	29.4
600-TiO_2	600	99.8	ND	0.02	0	a	34.2	45.0
700-TiO_2	700	–	ND	ND	0	80% a, 20% r	22.1	72.6
800-TiO_2	800	–	–	–	–	34% a, 66% r	3.17	450.6
P-25	1200	–	ND	0	0	r	48.4	29.5
80-Mn-1	80	78.8	–	5.21	0.83	am	386	6.0
400-Mn-1	400	–	–	–	–	am	247	9.3
500-Mn-1	500	–	–	–	–	69.3% a, 30.7% r	125	12
600-Mn-1	600	98.7	ND	ND	1.02	66% a, 34% r	16	94
800-Mn-1	800	–	–	–	–	r	0.90	1590
80-Mn-5	80	–	–	–	–	am	430	5.4
400-Mn-5	400	–	–	–	–	am	272	8.5
500-Mn-5	500	–	–	–	–	r	160	8.9
600-Mn-5	600	93.2	ND	ND	5.24	r (tr) $MnTiO_3$	3.29	430
800-Mn-5	800	–	–	–	–	r, Mn_2O_3	0.56	2550
80-Mn-30	80	–	–	–	–	am	479	4.8
400-Mn-30	400	–	–	–	–	am	276	8.4
500-Mn-30	500	–	–	–	–	am	202	11.4
550-Mn-30	550	–	–	–	–	r	120	11.9
600-Mn-30	600	615	ND	ND	29.83	r, Mn_2O_3	40	36
800-Mn-30	800	–	–	–	–	r, Mn_2O_3	5.37	266

am = amorphous phase, a = anatase, r = rutile, ND = not detected.

rather effective process. The degree of manganese extraction into a combined X-ray amorphous precipitate is 99.9% at a degree of modification with Mn from 1 to 5 wt % and decreases to 96% at 30 wt % Mn (Fig. 1).

According to XRD and thermal analysis data (Table 1, Figs. 2–4), hydrolysis in the $TiCl_4$–$MnCl_2$–NH_4OH–H_2O system led to the formation of X-ray amorphous materials, which remained amorphous up to 400°C. Modification of TiO_2 with 1–30 wt % Mn made it possible to obtain nanopowders ranging in particle size from 2.6 to 7.6 nm and in specific free surface area from 876 to 303 m^2/g, respectively.

Phase formation. Raising the heat treatment temperature of the hydrolysis products led to a reduction in the specific surface area of the powders (Fig. 5), which was especially accelerated by anatase (and then rutile), manganese oxide, and manganese metatitanate crystallization processes, as well as by crystallite aggregation and agglomeration.

Thermal analysis of the air-dry (~20°C) hydrolysis products (Fig. 3, Table 2) yielded differential scanning calorimetry (DSC) curves similar to that of pure titanium oxyhydroxide, with one endothermic peak and one considerable exothermic peak. Dehydration of the

Table 2. Thermal events and XRD data in the Ti–O–Mn system

Sample	t_{min}, °C	t_{max}, °C	ΔM, % (TG data at t_{max})	d, Å at t_{max}	Phase composition
	DSC			XRD	
TiO_2	145.8	412.2	–23.3	3.52, 2.36	Anatase
		700	–	3.24, 2.49	Rutile
		–	–	–	$a = 4.559$, $c = 2.959$
MnO_2 [22, 23]	575	–	–14.1	–	Mn_2O_3
	900	–	–4.2	–	Mn_3O_4
Mn-1	139.9	469.7	–23.8	3.52, 2.36	Anatase
		–	–	3.24, 2.49	Rutile
		787.1	–	3.24, 2.49	Rutile
		–	–	–	$a = 4.559$, $c = 2.959$
Mn-5	137.2	508.1	–23.63	3.24, 2.49	Rutile
		–	–	–	$a = 4.59$, $c = 2.959$
		550.0	+0.50	3.24, 2.49	Rutile
		600		3.76, 2.76, 2.56	$MnTiO_3$ (tr)
		800		3.24, 2.49	Rutile
		–		3.85, 2.73, 2.49	Mn_2O_3
		923	–0.69	3.24, 2.49	Rutile
		–	–	3.76, 2.76, 2.56	$MnTiO_3$
Mn-30	134.9	559.1	–19.96	3.22, 2.47	Rutile
		–	–	–	$a = 4.548$,
		600	+1.18	–	$c = 2.946$
		–	–	3.85, 2.73, 2.49	Rutile
		–	–	–	$a = 4.59$,
		932.7	–2.91	–	$c = 2.959$
		–	–	3.76, 2.78, 2.56	Mn_2O_3 Rutile $MnTiO_3$

hydrolysis products, accompanied by the largest weight loss, in all cases resulted in endothermic peaks with minima in a temperature range as narrow as 134.9–139.9°C.

According to chemical analysis data for the powders heat-treated at 80°C, they consisted largely of the titanium oxyhydroxide $TiO(OH)_2$, which lost 19 to 22% water and volatile components (NH_4OH and HCl), captured together with the mother liquor, as the hydrolysis temperature was raised, to the point of the formation and crystallization of an anatase and/or rutile TiO_2 phase. As the degree of modification increases from 1 to 5 and 30 wt % Mn, the temperature of the first phase transition, corresponding to the maxima of the exothermic peaks, respectively, rises from 459.7 to 508.1 and 559.1°C (Fig. 3, Table 2).

Note that, according to the XRD data (Fig. 2, Table 1), the only significant exothermic peak corresponded to the formation of an anatase + rutile mixture in sample Mn-1 and to the formation of rutile and manganese oxide (Mn_2O_3) in the case of modification with ≥5 wt % Mn. In this phase formation region, the TG curves showed a distinguishable narrow weight gain range, indicative of oxidation processes, followed by a weight loss, attributable to manganese oxidation, followed by oxygen release from the manganese oxides

Table 3. Textural characteristics of the TiO_2- and Mn-based composites as functions of manganese content and heat treatment temperature

Sample	Phase composition (XRD)	S, m^2/g	V, cm^3/g	h, nm	D, nm
20-Mn-1	am	303	0.2577	3.40	3.79
80-Mn-1	am	395	0.2875	2.91	3.75
400-Mn-1	am	250	0.272	4.41	4.14
500-Mn-1	69% a, 31% r	125	0.269	8.59	7.22
600-Mn-1	66% a, 34% r	16	0.041	10.44	11.44
800-Mn-1	r	0.9	0.0015	6.55	27.16
20-Mn-5	am	458	0.3777	3.30	3.65
80-Mn-5	am	430	0.3294	3.06	3.51
400-Mn-5	am	272	0.317	4.67	4.27
500-Mn-5	r	160	0.3256	8.15	6.87
600-Mn-5	r, $MnTiO_3$ (tr)	3.29	0.0078	9.47	16.55
800-Mn-5	r, Mn_2O_3	0.56	0.00082	5.84	28.38
20-Mn-30	am	876	0.9302	4.25	4.82
80-Mn-30	am	479	0.5668	4.73	5.03
400-Mn-30	am	276	0.507	7.35	6.61
500-Mn-30	am	202	0.5179	10.28	8.84
600-Mn-30	r, Mn_2O_3	40	0.151	15.26	16.93
800-Mn-30	r, Mn_2O_3	5.37	0.0787	5.86	18.13

[38–40]. The DSC curves of samples Mn-5 and Mn-30 (Fig. 3, Table 2) showed additional, relatively small endothermic peaks, having minima at 923.0 and 932.7°C. In the case of pure manganese dioxide, the endothermic peaks observed at 575 and 900°C [41] were due to oxygen loss and manganese oxidation from Mn^{2+} to Mn^{3+} and Mn^{4+} as a result of the following sequence of transformations:

$$MnO_2 \rightarrow Mn_2O_3 \rightarrow Mn_3O_4.$$

In the case of the composites under investigation, the endothermic peaks can be interpreted as evidence of oxygen loss upon the formation of manganese metatitanate ($MnTiO_3$), as supported by XRD data (Fig. 2, Table 2) and the noticeable weight loss observed in the TG curve of the samples in this temperature range.

One possible sequence of transformations of phase states of the manganese in the composite is as follows [30]:

$$Mn(OH)_2 + O_2 \rightarrow MnO_2 + H_2O$$
$$\rightarrow Mn_2O_3 + O_2 \uparrow \rightarrow MnTiO_3 + O_2 \uparrow .$$

It is worth noting that, in the highly modified sample Mn-30, a more compressed rutile crystal lattice (3.22 Å) was first formed, with unit-cell parameters $a = 4.548$ Å and $c = 2.946$ Å, against the $a = 4.559$ Å and $c = 2.959$ Å of rutile (3.24 Å), to which it was reduced after separation of the manganese-containing phases Mn_2O_3 and $MnTiO_3$.

The present results confirm that manganese cations have a promoting effect [29] on the anatase-to-rutile transformation (Table 2). In particular, samples Mn-1 were found to contain rutile along with anatase after heat treatment of the X-ray amorphous material at a temperature as low as 500°C, whereas in the pure $TiCl_4$ hydrolysis product of the same origin the rutile phase was only detected after heat treatment at temperatures above 700°C. The anatase-to-rutile transformation reached completion at a temperature of

Table 4. PCA (E) of the TiO_2- and Mn-based composites

Sample	Phase composition	S, m^2/g	E, % at $\lambda > 400$ nm for		
			ferroin	MB	aniline
P-25	85% a, 15% r	48.4	0	1.2	1.2
400-Mn-1	am	246.9	25.9	58.6	8.3
500-Mn-1	69.3% a, 30.7% r	–	3.5	3.2	–
600-Mn-1	66% a, 34% r	16.0	2.5	3.6	34.1
800-Mn-1	r	0.90	6.9	0.8	45.9
400-Mn-5	am	271.9	18.5	62.2	19.8
500-Mn-5	r	–	3.8	2.6	–
600-Mn-5	r, $MnTiO_3$ (tr)	3.29	1.5	1.0	30.4
800-Mn-5	r, Mn_2O_3	0.56	7.1	0.4	61.23
400-Mn-30	am	276	16.5	41.6	10.1
500-Mn-30	am	–	14.8	49.6	–
550-Mn-30	r	–	10.3		–
600-Mn-30	r, Mn_2O_3	39.7	3.6	2.2	14.21
800-Mn-30	r, Mn_2O_3, $MnTiO_3$	5.37	6.1	2.2	32.56

am = amorphous phase, a = anatase, r = rutile.

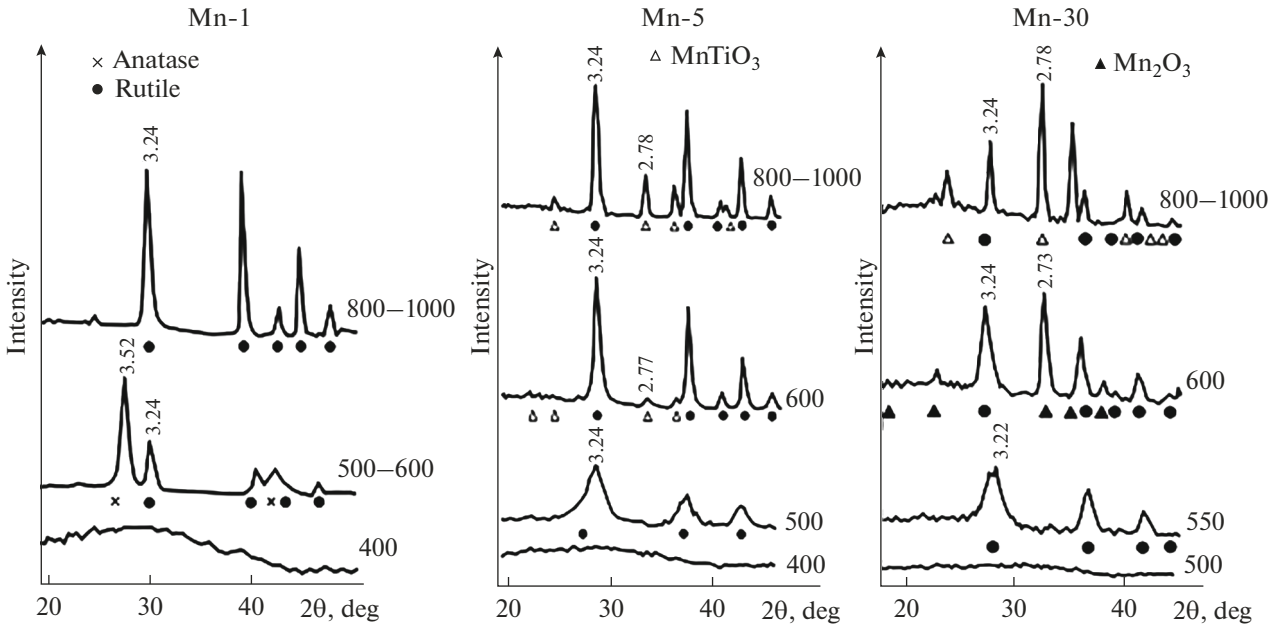

Fig. 2. X-ray diffraction patterns of Mn-modified titanium dioxide at various heat treatment temperatures (numbers at the scans, °C) and percentages of Mn (the estimated instrumental error limits in our X-ray count rate measurements were within ±0.5%).

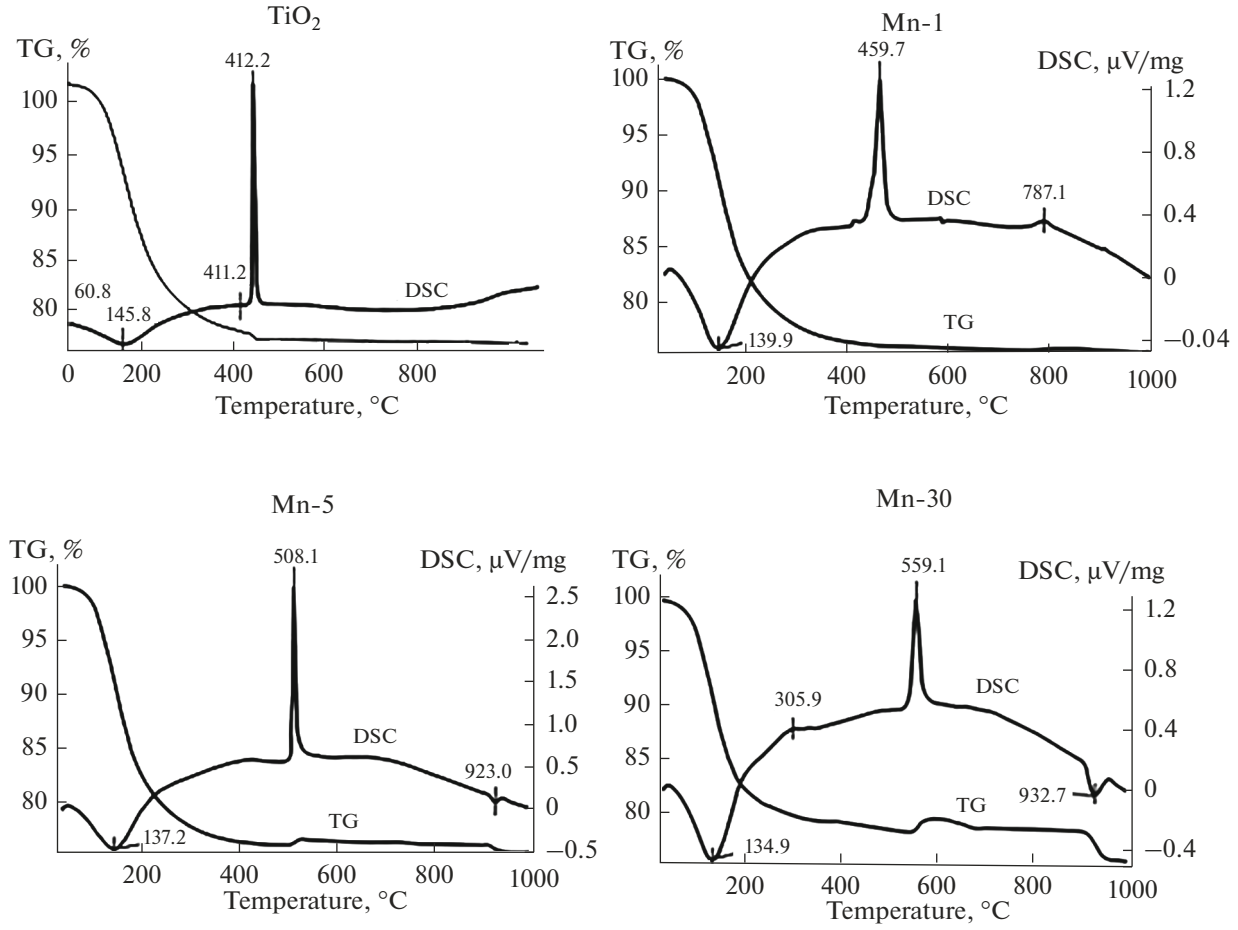

Fig. 3. Thermal analysis data for TiO_2 and the Mn-modified TiO_2 samples differing in manganese content (the estimated relative error limits in our temperature measurements in the range 30 to 770 K were ±1.5%, and the estimated relative error limits in our weight measurements were ±1%).

800°C. In the synthesis products containing ≥5 wt % Mn, rutile was formed directly from the X-ray amorphous material, without formation of anatase as a metastable state. This was accompanied by crystallization of manganese oxide phases (Mn_2O_3 at 600°C and $MnTiO_3$ at 800°C).

Thus, a characteristic feature of the synthesis products in the Ti–O–Mn system is the formation of several multiphase zones, depending on modification and heat treatment temperature (Fig. 4), with the following possible phase transitions: X-ray amorphous material → anatase → rutile + Mn_2O_3 → rutile + $MnTiO_3$. In the highly modified synthesis products, the following phase transitions were detected: X-ray amorphous material → rutile + trace levels of $MnTiO_3$ → rutile + Mn_2O_3 → rutile + $MnTiO_3$.

Texture. Like that of the pure titanium dioxide, the specific surface area of the Mn-modified synthesis products was found to decrease systematically with increasing heat treatment temperature (Fig. 5, Table 1). The X-ray amorphous powders had a specific surface area as large as 202–479 m^2/g and consisted of nanoparticles ranging in size from 11.4 to 4.8 nm. The onset of the formation of the anatase and rutile phases at temperatures from 500 to 550°C was accompanied by a decrease in the specific surface of the powders to 120–160 m^2/g and a slight increase in crystallite size, to 8.9–11.9 nm. On the completion of rutile formation and the separation of the Mn-containing phases Mn_2O_3 and $MnTiO_3$ at temperatures from 600 to 800°C, the specific surface area dropped to 0.56–40 m^2/g.

It is seen in Fig. 5 that all of the TiO_2/Mn composite samples had a larger specific surface area than did pure TiO_2 of similar origin.

The sorption isotherms of both the X-ray amorphous and crystalline samples obtained at heat treatment temperatures in the range 20–500°C have an absorption–desorption character and are S-shaped, with well-defined hysteresis loops (Fig. 6), which, according to the

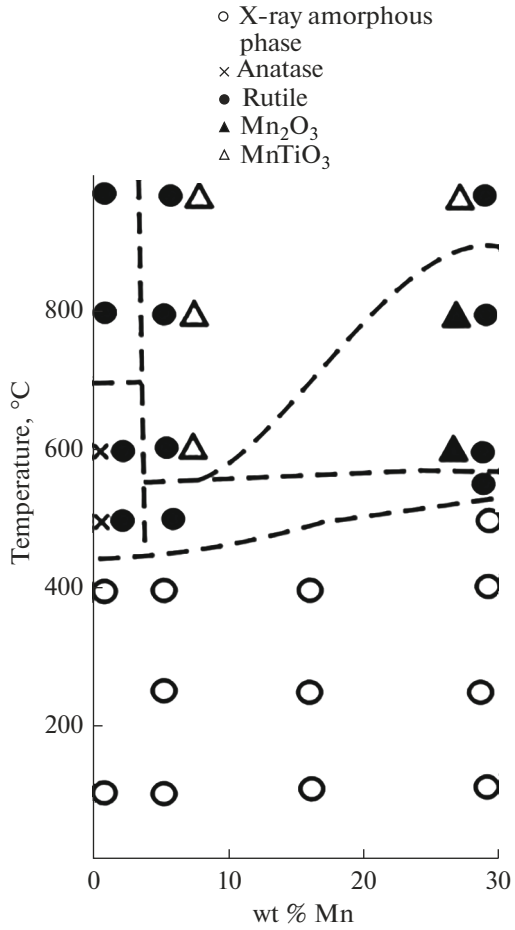

Fig. 4. Phase composition of the Mn-modified titanium dioxide powders heat-treated at temperatures of up to 1000°C (the estimated instrumental error limits in our X-ray count rate measurements were within ±0.5%).

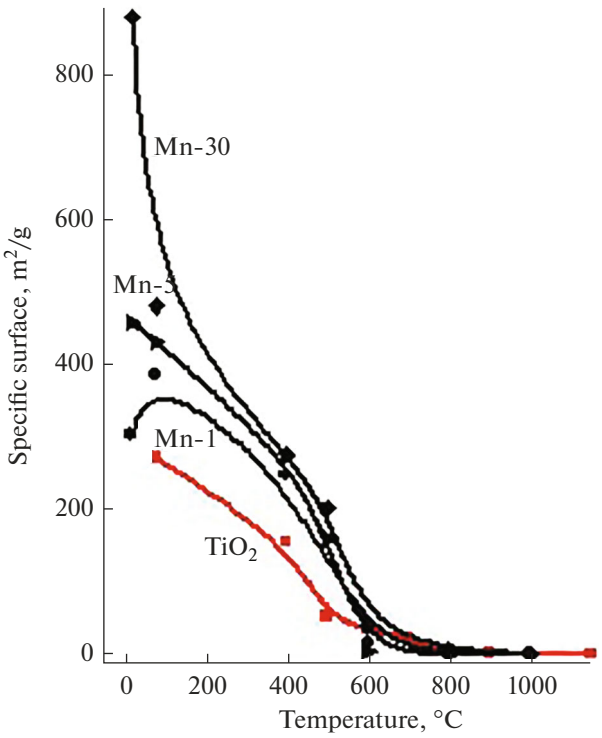

Fig. 5. Specific surface area of TiO_2 and the Mn-modified TiO_2 samples as a function of manganese content and heat treatment temperature (the estimated relative error limits in our specific surface area measurements were ±5%).

relevant IUPAC classification [41], indicates that the synthesized materials are mesoporous.

The temperature dependences of the pore volume (V), depth (h), and diameter (D) have a rather extreme character (Table 3). The parameter h reaches a maximum level near 600°C, and D, at 800°C. The samples heat-treated at 500°C or lower temperatures were comparable in pore depth and diameter. As the temperature was raised to above 600°C, the pore diameter increased more rapidly than the pore depth, pointing to surface smoothing.

The effect of temperature on the variation in the V of micropores is similar to that in the case of the specific surface area, which is probably a consequence of the active water removal from the oxyhydroxide hydrolysis products. In the X-ray amorphous materials (<500°C), V ranged from 0.25 to 0.93 cm^3/g, increasing with increasing manganese content and powder particle size. As the temperature was raised further, V dropped sharply, which was associated with the crystallization, aggregation, and, finally, agglomeration processes at temperatures above 800°C. In particular, the micropore volume in sample 500-Mn-1 was 0.2690 cm^3/g, whereas that in sample 800-Mn-1 was just 0.0015 cm^3/g. At the same time, it is worth noting that increasing the percentage of Mn stabilized the micropore size at elevated temperatures.

Thus, in the Ti–O–Mn system both X-ray amorphous and crystalline multiphase composites with a specific surface area from 49 to 876 m^2/g have a mesoporous structure. Mesoporous materials are thought to be very promising catalysts for transformations of voluminous organic molecules because the presence of mesopores can help overcome diffusional limitations characteristic of micropores.

PCA. We evaluated the PCA of the samples heat-treated in the range 400–800°C, where crystalline phases were already formed in most cases and S remained relatively large.

Manganese incorporated into titanium dioxide determines its spectral sensitization in the visible region. In particular, all of the synthesized materials were shown to exhibit higher PCA compared to the commercially available photocatalyst P-25.

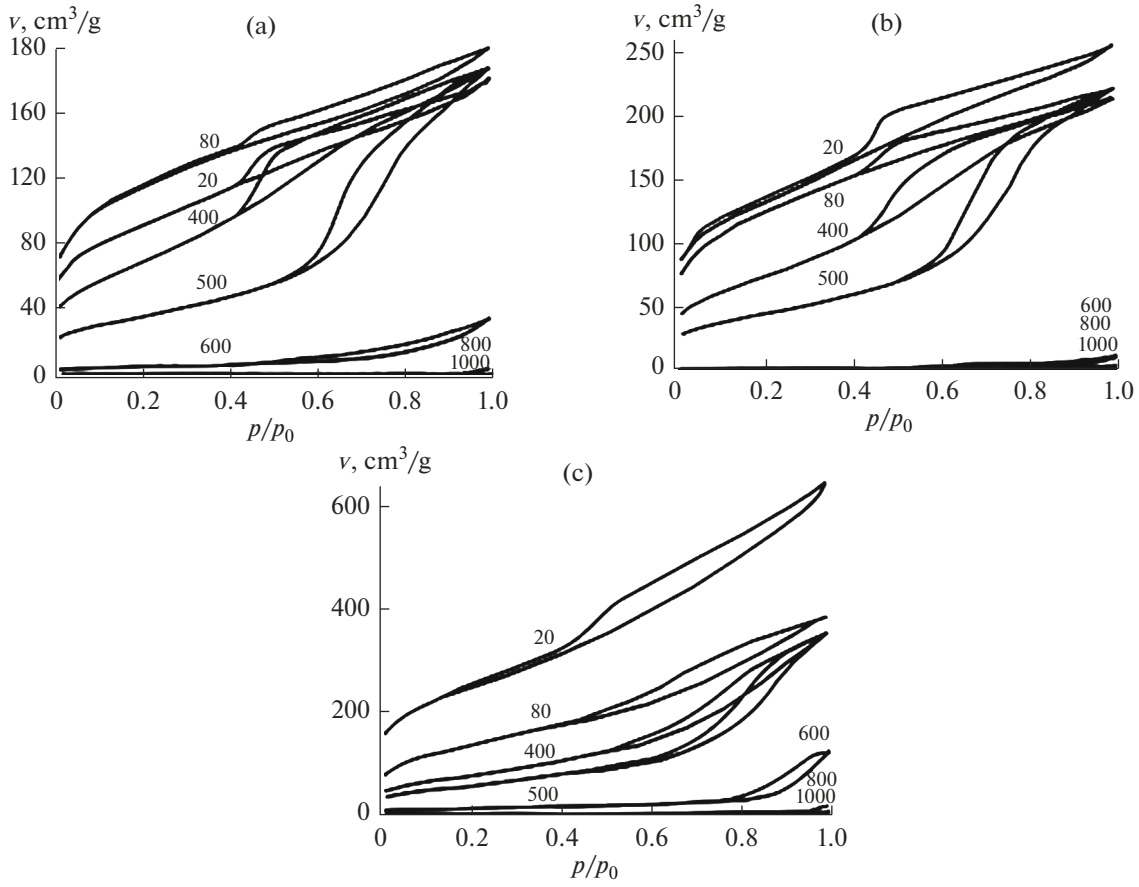

Fig. 6. Sorption isotherms of the Mn-modified titanium dioxide samples containing (a) 1, (b) 5, and (c) 30 wt % Mn and calcined at various temperatures (numbers at the curves, °C) (the estimated relative error limits are ±5%).

The PCA data presented in Table 4 and Fig. 7 reflect the joint effect of modifier content and a combination of structural components and powder texture, which are nonlinear functions of heat treatment conditions and the subject of degradation. For example, PCA values that are not always high are determined by the larger specific surface area of the samples heat-treated at a temperature of 500°C in comparison with 600 and even 800°C, which is particularly well illustrated by the example of aniline degradation (Fig. 7).

The PCA of the synthesis products depended strongly on the nature of the subject of destruction. In particular, the degree of ferroin and MB degradation at heat treatment temperatures above 500°C did not exceed 3.6%, whereas under similar conditions aniline decomposed almost completely, to 61%.

In addition, the following general trends were noticed:

At a heat treatment temperature of 400°C, the PCA of the powders for ferroin and MB degradation (Table 4, Fig. 7) was rather high, and it decreased sharply with increasing heat treatment temperature. The only exception was the sample containing 30 wt % Mn, whose PCA persisted between 500 and 600°C. In contrast, in the case of the photocatalytic destruction of aniline, all of the samples exhibited low PCA at a heat treatment temperature of 400°C, which increased with increasing temperature, reaching a maximum level at 800°C.

The PCA of the materials studied here had a selective character for different dyes, in agreement with previously reported data [42–44]. The very likely reason for this is that the subjects of decomposition differ in redox potential [45–47]. In addition, the materials used as photocatalysts differ in charge. Further research is needed to assess the influence of these parameters on PCA selectivity and effectiveness.

It is also worth noting that, according to Opra et al. [32], the synthesized photocatalytic materials based on manganese-modified titanium dioxide are potentially attractive as anode materials for lithium ion batteries having high reversible and specific capacity.

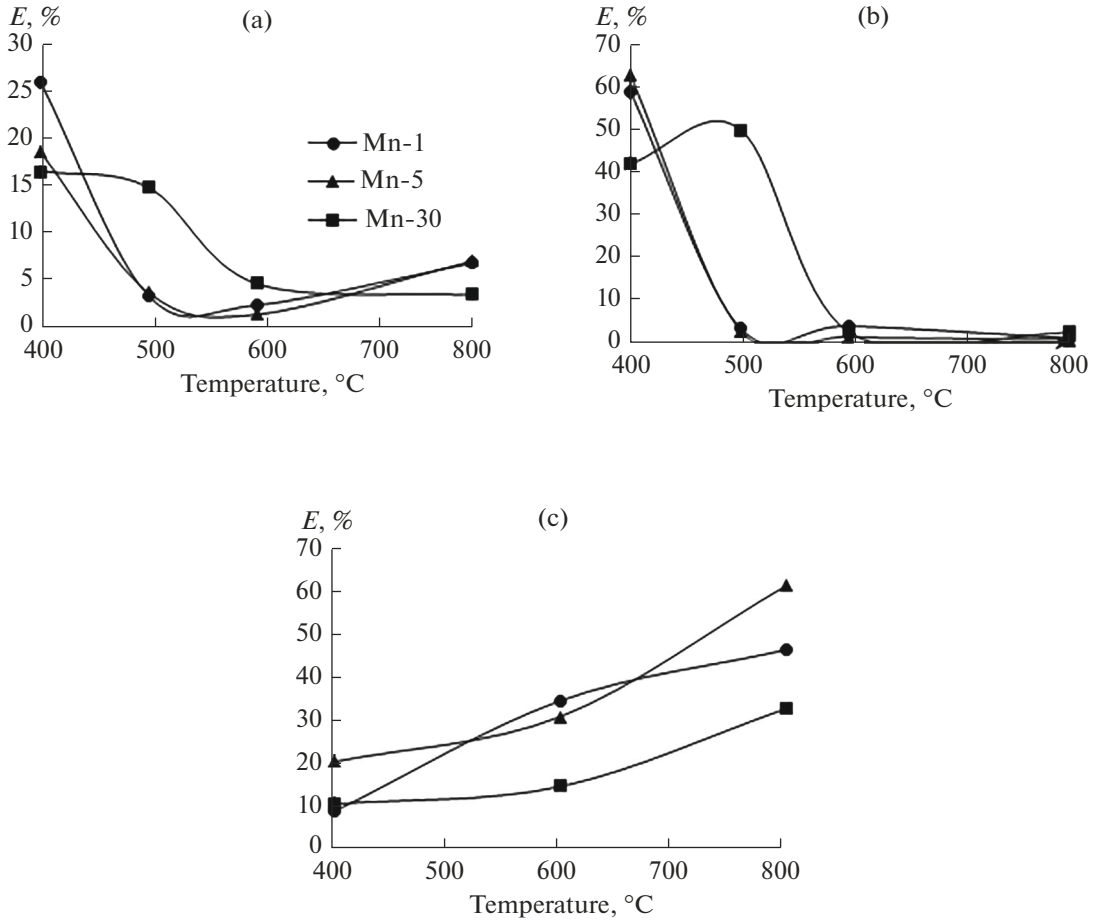

Fig. 7. PCA (E) as a function of Mn content for the Mn-modified titanium dioxide powders at various temperatures: (a) ferroin, (b) MB, and (c) aniline (the estimated absolute error limits of the spectrophotometer in our directional transmittance measurements were ±1%).

CONCLUSIONS

We have synthesized photocatalytic materials based on manganese-modified titanium dioxide and studied their physicochemical and photocatalytic properties at manganese concentrations from 1 to 30 wt % and heat treatment temperatures from 400 to 800°C.

The photocatalysts obtained in this study have higher PCA under illumination with visible light than does the commercially available photocatalyst Degussa P-25.

The PCA of the materials studied here has a selective character for different dyes, which seems to be determined by the surface charge of the materials and the redox potentials of the dyes.

The synthesized materials have a rather high PCA for aniline destruction, which increases with increasing heat treatment temperature.

CONFLICT OF INTEREST

The authors declare that they have no conflicts of interest.

REFERENCES

1. Fujishima, A. and Honda, K., Electrochemical photolysis of water at a semiconductor electrode, *Nature,* 1972, vol. 238, no. 5358, pp. 37–38. https://doi.org/10.1038/238037a0
2. Dong, H., Zeng, G., Tang, L., Fan, C., Zhang, C., and He, X., An overview on limitations of TiO_2-based particles for photocatalytic degradation of organic pollutants and the corresponding countermeasures, *Water. Res.,* 2015, vol. 79, pp. 128–146. https://doi.org/10.1016/j.watres.2015.04.038
3. Jiang, L., Wang, Y., and Feng, C., Application of photocatalytic technology in environmental safety, *Procedia Eng.,* 2012, vol. 45, pp. 993–997. https://doi.org/10.1016/j.proeng.2012.08.271
4. Tasbihi, M., Călin, I., Šuligoj, A., Fanetti, M., and Lavrenčič Štangar, U., Photocatalytic degradation of gaseous toluene by using TiO_2 nanoparticles immobilized on fiberglass cloth, *J. Photochem. Photobiol., A,* 2017, vol. 336, pp. 89–97. https://doi.org/10.1016/j.jphotochem.2016.12.025
5. Bhattacharyya, A., Kawi, S., and Ray, M.B., Photocatalytic degradation of orange II by TiO_2 catalysts sup-

ported on adsorbents, *Catal. Today,* 2004, vol. 98, no. 3, pp. 431–439.
https://doi.org/10.1016/j.cattod.2004.08.010

6. Jacoby, W.A., Maness, P.C., Wolfrum, E.J., Blake, D.M., and Fennell, J.A., Mineralization of bacterial cell mass on a photocatalytic surface in air, *Environ. Sci. Technol.,* 1998, vol. 32, no. 17, pp. 2650–2653.
https://doi.org/10.1021/es980036f
7. Caballero, L., Whitehead, K.A., Allen, N.S., and Verran, J., Inactivation of *Escherichia coli* on immobilized TiO_2 using fluorescent light, *J. Photochem. Photobiol., A,* 2009, vol. 202, no. 2, pp. 92–98.
https://doi.org/10.1016/j.jphotochem.2008.11.005
8. Liu, H.-L. and Yang, Th. C.-K., Photocatalytic inactivation of *Escherichia coli* and *Lactobacillus helveticus* by ZnO and TiO_2 activated with ultraviolet light, *Process Biochem.,* 2003, vol. 39, no. 4, pp. 475–481.
https://doi.org/10.1016/S0032-9592(03)00084-0
9. Burton, P., Peterson, E., Boyle, T., et al., Synthesis of high surface area ZnO(0001) plates as novel oxide supports for heterogeneous catalysts, *Catal. Lett.,* 2010, vol. 139, no. 1, pp. 26–32.
https://doi.org/10.1007/s10562-010-0405-1
10. Bignozzi, C.A., Caramori, S., Cristino, V., et al., Nanostructured photoelectrodes based on WO_3: applications to photooxidation of aqueous electrolytes, *Chem. Soc. Rev.,* 2013, vol. 42, no. 6, pp. 2228–2246.
https://doi.org/10.1039/c2cs35373c
11. Tian, L., Ye, L., Liu, J., et al., Solvothermal synthesis of CNTs–WO_3 hybrid nanostructures with high photocatalytic activity under visible light, *Catal. Commun.,* 2012, vol. 17, pp. 99–103.
https://doi.org/10.1016/j.catcom.2011.10.023
12. Franking, R., Li, L., Lukowski, M.A., et al., Facile post-growth doping of nanostructured hematite photoanodes for enhanced photoelectrochemical water oxidation, *Energy Environ Sci.,* 2013, vol. 6, no. 2, pp. 500–512.
https://doi.org/10.1039/C2EE23837C
13. Bang, J.U., Lee, S.J., Jang, J.S., et al., Geometric effect of single or double metal-tipped CdSe nanorods on photocatalytic H_2 generation, *J. Phys. Chem. Lett.,* 2012, vol. 3, no. 24, pp. 3781–3785.
https://doi.org/10.1021/jz301732n
14. Wang, J., Yin, S., Zhang, Q., et al., Mechanochemical synthesis of fluorine-doped $SrTiO_3$ and its photo-oxidation properties, *Chem. Lett.,* 2003, vol. 32, no. 6, pp. 540–541.
https://doi.org/10.1246/cl.2003.540
15. Kirovskaya, I.A., Timoshenko, O.T., and Karpova, E.O., The catalytic and photocatalytic properties of InP–CdS and ZnTe–CdS system components, *Russ. J. Phys. Chem. A,* 2011, vol. 85, no. 4, pp. 557–560.
https://doi.org/10.1134/S0036024411030186
16. Phuruangrat, A., Sakhon, T., Kuntalue, B., et al., Characterization of visible-light-induced $BiVO_4$ photocatalyst synthesized by chemical combustion method fueled by tartaric acid, *Russ. J. Inorg. Chem.,* 2021, vol. 66, pp. 1829–1836.
https://doi.org/10.1134/S0036023621120135
17. Chomkitichai, W., Jansanthea, P., and Channei, D., Photocatalytic activity enhancement in methylene blue degradation by loading Ag nanoparticles onto α-Fe_2O_3, *Russ. J. Inorg. Chem.,* 2021, vol. 66, pp. 1995–2003.
https://doi.org/10.1134/S0036023621130027
18. Dongmei He, Du, L., Wang, K., et al., Efficient process of ALD CuO and its application in photocatalytic H_2 evolution, *Russ. J. Inorg. Chem.,* 2021, vol. 66, pp. 1986–1994.
https://doi.org/10.1134/S0036023621130040
19. Dumrongrojthanath, P., Phuruangrat, A., Sakhon, T., et al., Effect of Gd dopant on visible-light-driven photocatalytic properties of CeO_2 nanowires synthesized microwave-assisted hydrothermal method, *Russ. J. Inorg. Chem.,* 2022, vol. 67, pp. 1880–1887.
https://doi.org/10.1134/S0036023622600757
20. Shtareva, A.V., Shtarev, D.S., Balanov, M.I., et al., Bismuthyl carbonate heterostructures are a way to enhance the photocatalytic activity of alkaline-earth bismuthates, *Russ. J. Inorg. Chem.,* 2022, vol. 67, pp. 1375–1385.
https://doi.org/10.1134/S0036023622090157
21. Shtarev, D.S., Shtareva, A.V., and Petrova, A.Y., Effects of the dopant type and concentration on the photocatalytic activity of strontium bismuthate $Sr_2Bi_2O_5$, *Russ. J. Inorg. Chem.,* 2022, vol. 67, pp. 1368–1374.
https://doi.org/10.1134/S0036023622090145
22. Bhatkhande, D.S., Pangarkar, V.G., and Beenackers, A.A.C.M., Photocatalytic degradation for environmental applications – a review, *J. Chem. Technol. Biotechnol.,* 2002, vol. 77, no. 1, pp. 102–116.
https://doi.org/10.1002/jctb.532
23. Yu, J.C., Ho, W., Yu, J., Yip, H., Wong, P.K., and Jincai, Z., Efficient visible-light-induced photocatalytic disinfection on sulfur-doped nanocrystalline titania, *Environ. Sci. Technol.,* 2005, vol. 39, no. 4, pp. 1175–1179.
https://doi.org/10.1021/es035374h
24. Wang, W., Huang, G., Yu, J.C., and Wong, P.K., Advances in photocatalytic disinfection of bacteria: development of photocatalysts and mechanisms, *J. Environ. Sci.,* 2015, vol. 34, pp. 232–247.
https://doi.org/10.1016/j.jes.2015.05.003
25. Karvinen, S.M., The effects of trace element doping on the optical properties and photocatalytic activity of nanostructured titanium dioxide, *Ind. Eng. Chem. Res.,* 2003, vol. 42, no. 5, pp. 1035–1043.
https://doi.org/10.1021/ie020358z
26. Szczepanik, B., Photocatalytic degradation of organic contaminants over clay–TiO2 nanocomposites: a review, *Appl. Clay Sci.,* 2017, vol. 141, pp. 227–239.
https://doi.org/10.1016/j.clay.2017.02.029
27. Khan, H. and Berk, D., Synthesis, physicochemical properties and visible light photocatalytic studies of molybdenum, iron and vanadium doped titanium dioxide, *React. Kinet., Mech. Catal.,* 2014, vol. 111, no. 1, pp. 393–414.
https://doi.org/10.1007/s11144-013-0637-3
28. Devi, L.G., Nagaraju, K., Murthy, B.N., and Girish, K.S., Enhanced photocatalytic activity of transition metal ions Mn^{2+}, Ni^{2+} and Zn^{2+} doped polycrystalline titania for the degradation of Aniline Blue under UV/solar light, *J. Mol. Catal. A,* 2010, vol. 328, nos. 1–2, pp. 44–52.
https://doi.org/10.1016/j.molcata.2010.05.021

29. Anpo, M., Use of visible light. Second-generation titanium oxide photocatalysts prepared by the application of an advanced metal on-implantation method, *Pure Appl. Chem.,* 2000, vol. 72, no. 9, pp. 1787–1792. https://doi.org/10.1351/pac200072091787

30. Brus, V.V., Kovalyuk, Z.D., and Maryanchuk, P.D., Optical properties of TiO_2–MnO_2 thin films prepared by electron-beam evaporation, *Tech. Phys.,* 2012, vol. 57, no. 8, pp. 1148–1151. https://doi.org/10.1134/S1063784212080063

31. Ivanova, T. and Harizanova, A., Characterization of TiO and TiO–MnO oxides prepared by sol–gel method, *Solid State Ionics,* 2001, vol. 138, pp. 227–232. https://doi.org/10.1016/S0167-2738(00)00798-0

32. Opra, D.P., Gnedenkov, S.V., Sinebryukhov, S.L., et al., Manganese-doped titanium dioxide with improved electrochemical performance for lithium ion batteries, *Elektrokhim. Energ.,* 2019, vol. 19, no. 3, pp. 123–140. https://doi.org/10.18500/1608-4039-2019-19-3-123-140

33. Belikov, M.L., Sedneva, T.A., and Lokshin, E.P., Adsorptive and photocatalytic properties of tungsten-modified titanium dioxide, *Inorg. Mater.,* 2021, vol. 47, no. 2, pp. 146–153. https://doi.org/10.1134/S0020168521020023

34. Jin, Q., Arimoto, H., Fujishima, M., and Tada, H., Manganese oxide-surface modified titanium (IV) dioxide as environmental catalyst, *Catalysts,* 2013, vol. 3, no. 2, pp. 444–454. https://doi.org/10.3390/catal3020444

35. Sedneva, T.A., Lokshin, E.P., Belikov, M.L., and Kalinnikov, V.T., RF Patent 2435733, *Byull. Izobret.,* 2011, no. 34.

36. Sedneva, T.A., Lokshin, E.P., Belikov, M.L., and Belyaevskii, A.T., Synthesis and characterization of photocatalytic titanium(IV) oxide/cobalt(II) oxide nanocomposites, *Khim. Tekhnol.,* 2015, vol. 16, no. 7, pp. 398–407.

37. Matthews, R.W. and McEvoy, S.R., Destruction of phenol in water with sun, sand, and photocatalysis, *Sol. Energy,* 1992, vol. 49, no. 6, pp. 507–513. https://doi.org/10.1016/0038-092X(92)90159-8

38. Ivanova, V.P., Kasatov, B.K., Krasavina, T.N., and Rozinova, E.L., *Termicheskii analiz mineralov i gornykh porod* (Thermal Analysis of Minerals and Rocks), Leningrad: Nedra, 1974, p. 47.

39. Liptay, G., *Atlas of Thermoanalytical Curves,* Budapest: Academiai Kiado, 1973, vol. 2, p. 78.

40. Kazenas, K.E. and Tsvetkov, Yu.V., *Isparenie oksidov* (Vaporization of Oxides), Moscow: Nauka, 1997.

41. Gregg, S.J. and Sing, K.S.W., *Adsorption, Surface Area, and Porosity,* New York: Academic, 1982.

42. Parida, K.M. and Sahu, N., Visible light induced photocatalytic activity of rare earth titania nanocomposites, *J. Mol. Catal. A,* 2008, vol. 287, nos. 1–2, pp. 151–158. https://doi.org/10.1016/j.molcata.2008.02.028

43. Agafonov, A.V., Redozubov, A.A., Kozik, V.V., and Kraev, A.S., Photocatalytic activity of titania nanopowders prepared by a sol–gel process at various pHs, *Russ. J. Inorg. Chem.,* 2015, vol. 60, no. 8, pp. 906–912. https://doi.org/10.1134/S0036023615080021

44. Stepanov, A.Yu., Sotnikova, L.V., Vladimirov, A.A., et al., Synthesis and photocatalytic properties of TiO_2-based materials, *Vestn. Kemerovsk. Gos. Univ.,* 2013, vol. 1, no. 2, pp. 249–255.

45. Sabnis, R.W., Ross, E., Kothe, J., Naumann, R., et al., Indicator reagents, in *Ullmann's Encyclopedia of Industrial Chemistry.* Weinheim: Wiley, 2009, vol. 19, pp. 9–53. https://doi.org/10.1002/14356007.a14_127.pub2

46. Nayanova, E.V., Elipasheva, E.V., Sergeev, G.M., and Sergeeva, V.P., Redox properties of methylene blue as a promising photometric reagent for determination of halogen oxidants, *Anal. Kontrol,* 2015, vol. 19, no. 2, pp. 154–160. https://doi.org/10.15826/analitika.2015.19.2.005

47. Vakulin, I.V., Bugaets, D.V., and Zil'berg, R.A., Accuracy analysis for AM1, RM1, and PM7 semiempirical calculations of the redox potentials of substituted phenols, quinones, and anilines, *Butlerovsk. Soobshch.,* 2017, vol. 52, no. 11, pp. 53–59. https://doi.org/10.37952/ROI-jbc-01/17-52-11-53

Translated by O. Tsarev